

WFC3/UVIS CTE-EPER Measurement: Cycle 17 & 18

V. Kozhurina-Platais, B. Hilbert, S. Baggett, & L. Petro

September 27, 2011

Abstract

We present the results and measurement of Charge Transfer Efficiency (CTE) of the WFC3 UVIS detector, based on data acquired during the monthly internal Extended Pixel Edge Response (EPER) observations over a 2 year period. We present an algorithm for CTE assessment and fit a power-law to CTE measures versus signal level. We find that at each signal level, CTE declines linearly over time and CTE losses are worst at the lowest signal levels.

1. Introduction

The new instrument *Wide Field Camera 3* (WFC3) is a fourth - generation imaging instrument, installed in HST during Servicing Mission 4 in May 2009. The evaluation of the WFC3 UVIS CCD performance is one of the most important calibrations, in particular, the loss of Charge Transfer Efficiency. It is well-known that there is a significant loss of Charge Transfer Efficiency (CTE) for all HST CCDs in the environment of space as seen in: WFPC2 (Whitmore *et al.* 1999, Dolphin 2000), STIS (Gilliland *et al.* 1999; Goudfrooij & Kimble 2003; Goudfrooij *et al.* 2007) and ACS (Riess 2003; Mutchler & Siriani 2005). The CTE losses, due to cosmic rays damaging the silicon lattice, degrade the CCD detector performance with time. This degradation affects the precision of stellar photometry and astrometry on many HST science programs (Riess & Mack 2004; Kozhruina-Platais *et al.* 2007; Chiaberge *et al.* 2009). An analysis of the CTE losses in ACS images has

been presented in the form of analytical corrections for CTI-induced photometric losses in aperture photometry as a function of star positions on ACS/WFC CCD chips, flux, sky background, the time of observations and aperture size. Recently, Anderson & Bedin (2010) used an empirical approach to characterize the CTE losses in ACS/WFC images. They developed a pixel-based correction for CTI induced flux loss and centroid shift in ACS/WFC images; a similar correction may also be implemented for WFC3/UVIS images.

The first WFC3/UVIS CTE evaluation based on external calibrations of the rich open cluster NGC6791 (Kozhurina-Platais *et al.* 2011) showed a clear trend, with Charge Transfer Inefficiency increasing from 2% in October 2009 to 7% in the fall 2010 for the low-sky background ($\sim 0.1\text{--}1.0\ e^-$) and the flux range from 500 to 2000 e^- .

A popular technique of CTE measurement is the Extended Pixel Edge Response (*EPER*) described by Janesick (2001). *EPER* measures the excess charge in the CCD overscan pixels (also referred to as extended pixel region), which decreases exponentially with distance from the science pixels. The *EPER* technique has been successfully used for the ACS Wide Field Camera and High Resolution Camera to measure and monitor the CTE (Mutchler & Sirianni, 2005). The same technique was used by Robberto (2007) to measure the CTE for the *WFC3 UVIS-2* detector during the ground-based ambient test campaign in April 2007 and by Kozhurina-Platais *et al.* (2009) for the WFC3 UVIS flight detector tested during the ground-based thermal vacuum campaign in April 2008.

Here, we present the results of two years of on-orbit of CTE measurements based on data acquired during the monthly internal *EPER* observations (CAL-11924, PI Kozhurina-Platais and CAL-12347, PI Kozhurina-Platais) with the internal TUNGSTEN lamp.

2. UVIS *EPER* Observations and its Depiction

The calibration program of CTE measurements consists of internal TUNGSTEN lamp flat field observations through the F390M, F390W and F438W filters, with integration times selected for a wide range of signal illumination levels, namely 200, 400, 800, 1600 and 5000 electrons. The flat fields with different signal levels are used to monitor the CTE losses with time by measuring the signal profiles into the trailing overscan region, as described by V.Kozhurina-Platais *et al.* 2009. Table 1 lists one set of the typical monthly observations with TUNGSTEN lamp, the filters, the exposure times, and the average signal levels in the flat field images.

Table 1: EPER monthly internal observing sequence.

Image ID	WFC3 UVIS Filters	Exp.Time (sec)	Intended Level (e^-)	Measured Level (e^-)
ibc620dmq	DARK	0.5	-	-
ibc620doq	F390M	9.2	200	164
ibc620dpq	F390M	22.9	400	424
ibc621zeq	DARK	0.5	-	-
ibc621zgq	F390W	6.4	800	834
ibc621zhq	F438W	7.6	1600	1700
ibc621zjq	F438W	22.7	5000	5113

The Flight Software does not allow for a true bias (with an exposure time equal to 0 seconds) to be taken in EPER mode, therefore each visit acquires 2 short-exposure dark frames which are used as a bias. During our EPER reductions it was noticed that some of the darks contain a low-level periodic noise component. The individual darks not affected by noise were stacked to construct a super-dark for calibrating the EPER internal flats. Similar to the noise in individual darks, some of the EPER observations were also contaminated with a periodic low-level electronic noise that had an amplitude, phase, and sign which varied from image to image. A sigma-clipping technique was used to remove the noise from the EPER observation, as described in Sec 3.

The noise issue is still under investigation; it is not seen in normal imaging mode and thus appears to be a consequence of the special EPER readout mode.

Before describing the data reduction techniques, we outline here the WFC3 CCD detector format and its structure as they relate to EPER measurements. As described in the WFC3 Instrument Handbook for Cycle 19 (L. Dressel *et al.* 2010), each of the UVIS CCD detectors has a size of 4096×2051 pixels. Both CCD chips have 25 extra columns on each side of the detector, which form the serial physical overscan regions. Each UVIS exposure also has 30×2 virtual serial overscan areas in the center of each row. Next to the inter-chip gap there are 19 rows of parallel overscan for each CCD chip. Figure 1 shows the format of a raw image obtained with full-chip four-amplifier readout.

For EPER measurements, the overscan regions have been modified and contain 300 pixels of serial overscan, and 300 pixels of parallel overscan for each CCD chip. Figure 2 shows the format of an EPER sub-array. As can be seen, the CCD EPER image area associated with each amplifier (indicated by yellow color) is only 1635×1770 pixels. Pixels which are not read out are shown in white. It is important to mention here, that only the **parallel** overscan is used for the EPER measurements and analysis in this report.

Fig. 1.— Schematic illustration of the standard WFC3 UVIS image from Figure 6.14 of the WFC3 Instrument handbook (L. Dressel *et al.* 2010). The pale yellow color indicates CCD image area (science pixels). The bright yellow color shows serial physical overscan and the pink color indicates serial virtual and parallel virtual overscan.

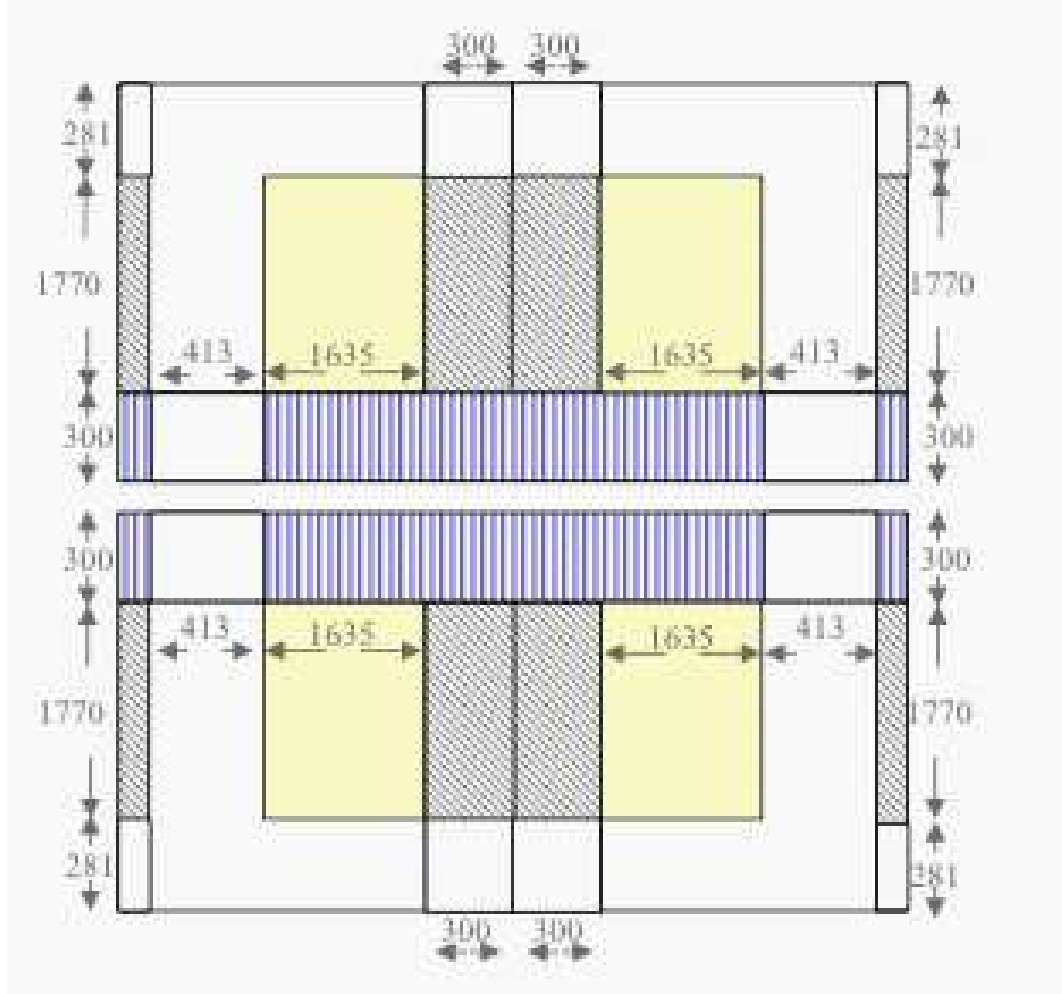


Fig. 2.— Schematic illustration of the EPER WFC3/UVIS sub-array from Robberto (2007, Figure 2). The yellow color indicates the CCD image area while the white color indicates areas that are not read out. The blue vertical stripes show the area of the parallel virtual overscan and the grey color denotes areas of serial virtual overscan.

3. UVIS EPER Measurements and Analysis

Following the EPER technique described by Janesick (2001), we measure the amount of deferred charge in the extended pixel region. Several columns are averaged to reduce noise and improve the signal-to-noise ratio in the extended pixel region. Then, CTE is calculated from the ratio of the total deferred charge in the extended pixel region S_D (in e^-) to the charge level of the last row of the active science pixels S_{LC} (in e^-), multiplied by N_p which is the number of signal transfers of the science pixels in the CCD register namely (Janesick, 2001, Eq. 5.21):

$$CTE_{EPER} = 1.0 - \frac{S_D}{S_{LC} \times N_p} \quad (1)$$

where for WFC3 $N_p = 2051$, the extended pixel region has size of 300 pixels for each amplifier (see Fig.2), and the last row of the trailing overscan region are $0, 0, 2070, 2070$ pixels for amplifier A, B, C, D respectively (see Fig.2). In order to increase the signal-to-noise ratio of the measurements, the signal in each row is averaged, creating a mean column for each amplifier.

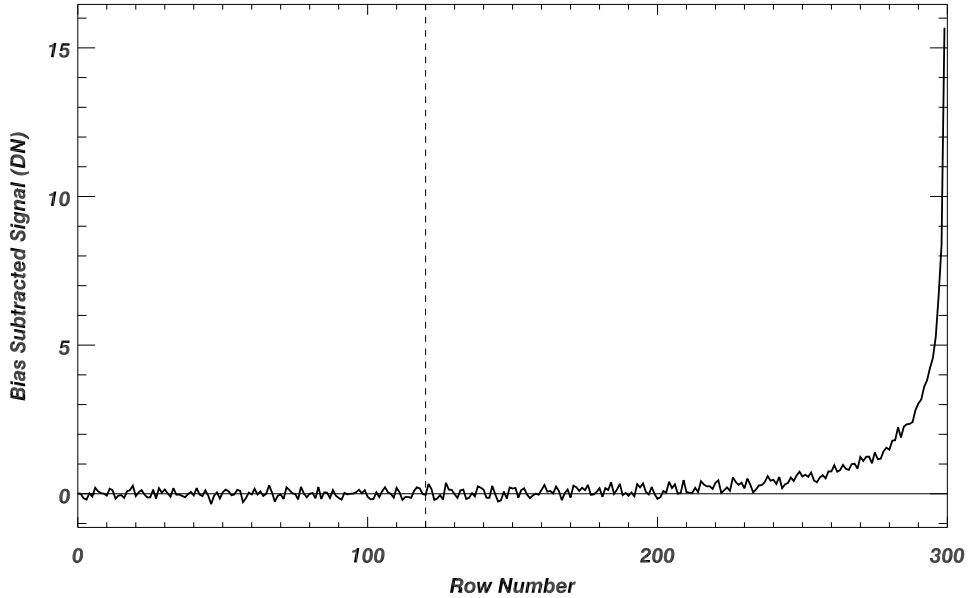


Fig. 3.— Typical profile of the deferred charge from UVIS EPER measurement for amplifier A . The vertical dashed line indicates the cutoff positions used in calculation of S_D .

Figure 3 shows the typical profile of the row-averaged deferred charge in the extended pixel region for amplifier A . As can be seen in Fig.3, the total deferred charge S_D is the sum of

the signal in the 180 overscan rows closest to the science pixels. S_{LC} is the signal in the last row of the science pixels, the signal present in row 301 in IDL convention and not shown in Fig.3. The trail of deferred charge decreases with increasing distance from the science pixels, and asymptotically approaches the bias level. In the case with the highest level of deferred signal, the tail of the signal reached the bias level about 180 rows into the extended overscan pixel region. Therefore, in each EPER image, S_D was calculated by summing the signal in 180 rows closest to the science pixels.

As described above (Sec. 2), some of the EPER observations were contaminated with a periodic low-level electronic noise that had an amplitude, phase, and sign which varied from image to image. Figure 4 shows an example of the noise as seen in the signal profile of the extended pixel region. The red diamonds indicate rows affected by the noise. When it was present, the noise always affected every 11th row. In Figure 4 there are in fact two distinct noise components, both with the 11 row periodicity, but offset from one another. This situation was not uncommon. In other images, one noise pattern was positive while the other was negative. In many cases, such as that in Figure 4, the magnitude of the noise was significant compared to the magnitude of the deferred charge that we would measure. Therefore prior to summing the signal in the extended pixel region, the noise must be filtered.

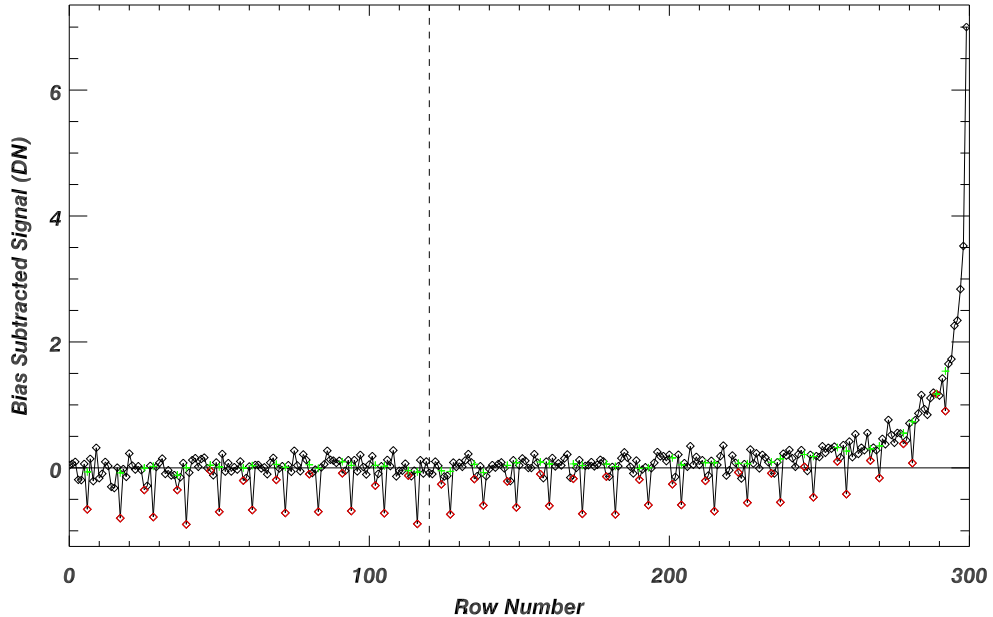


Fig. 4.— The same as Fig.3, but with noise in the deferred charge, a low-level electronic noise with a periodic component, different amplitudes, and sign. The red symbols show the periodic noise and the green after the filtering is applied.

Noise filtering. A sigma-clipping technique was used to identify and remove the noise from the data. First, we calculated the sigma-clipped standard deviation of the signals in rows 0 through 120 (i.e. the region outside of that we used to determine S_D) using IDL’s *robust_sigma.pro*. Next, we searched this region for rows with signal levels more than 3-sigma from zero. Since this region does not contain significant deferred charge from the science pixels, we could be assured that any rows identified with this technique had unusual signal levels that were due to noise. We knew that the noise had an 11-row frequency. The rows identified with our filter effectively provided the phase information. Thus, for a given image, if any rows in the row 0 - 120 region were flagged by the filter, we automatically flagged both with the 11 row periodicity on both sides of that row as noise-contaminated.

Once the locations of the noise-affected rows were identified, we removed the noise by replacing the signal level in each with the median of the signals in the two rows on either side. We also calculated the mean magnitude of the noise across all rows. In the case where the 11-row frequency indicated that row number 298 or 299 was affected by noise, we subtracted this mean noise magnitude from the observed signal level rather than replacing it with the median signal of the surrounding rows. With the steep profile of the signal on this side of the plot, and either zero or one row to the right of the affected row, it was not possible to calculate a reasonable median value. This entire technique was performed twice on each image, due to the observed presence of two separate noise patterns in some of the data. The results of the noise filtering can be seen as the green diamonds in Figure 4. For each row where noise was present, the signal in the red diamond was replaced with that in the green diamond. As shown in Figure 4, only the rows with noise are filtered and the rows without noise remain untouched.

Once this filtering was complete, we were confident that our summations of the deferred signals were more accurate than when the noise was present.

CTE calculation. After the filtering was applied, the EPER CTE is calculated using Eq.1. Figure 5 shows two years of the EPER CTE calculated from Eq.1 and uncertainties for each individual exposure as a function of the signal level in the last row of the trailing region (S_{LC}). Uncertainties were calculated by dividing the standard deviation of S_D by the denominator in Eq.(1). As can be seen from Figure 5, EPER CTE improved with increasing signal level and approached the ideal of 1.0 at high signals. The asymptotic distribution of CTE measurements is a clear evidence of a power law relationship between CTE and signal level, which can be defined in the following form:

$$CTE = 1 - m \times (S_{LC})^\rho \quad (2)$$

where ρ and m are free parameters and S_{LC} is the signal level of the last row in electrons. The numerical implementation of the power-law fitting was utilized by employing

a non-linear least-square fit using the IDL library by C. Markwardt (2006). The solid red line over-plotted on the CTE measurements (see Fig.5) as a function of the signal level is the best power-law fit for each individual exposure during the last two years. A similar asymptotic distribution of CTE *vs.* signal level also observed in ACS/WFC & HRC (Mutchler & Sirianni 2005) and STIS (Goudfrooij *et al.* 2006).

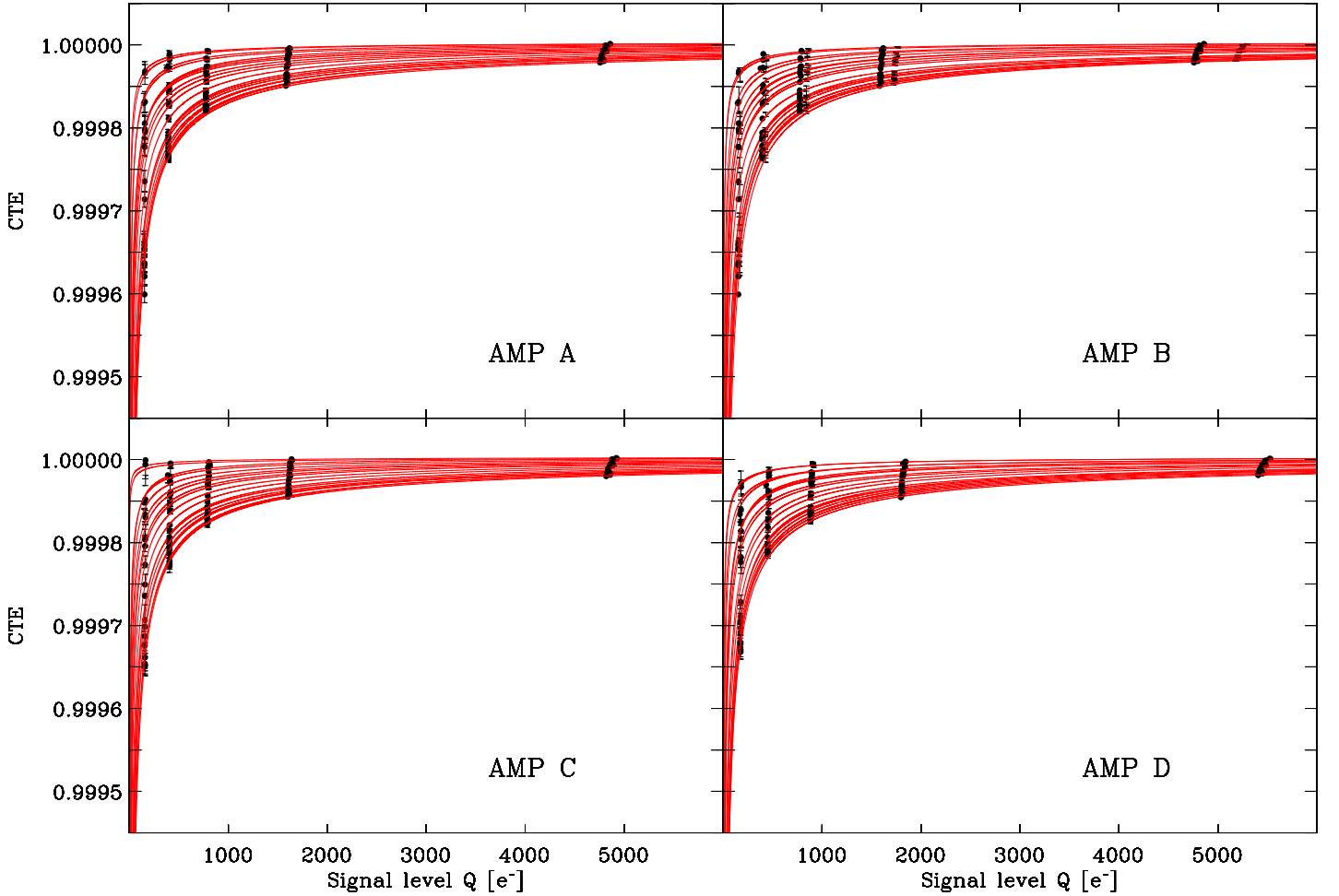


Fig. 5.— UVIS parallel CTE calculated for each individual exposure and for each amplifier. The over-plotted red line is the best power-law fit for each observation during the two years 2009–2011.

CTE can also be characterized in terms of charge transfer inefficiency (CTI), which is the fraction of charge left behind in a single pixel transfer i.e. $CTI = (1 - CTE)$. Then, Eq.2 can be rewritten as a linear \log - \log with the parameters m and ρ , namely:

$$\log(CTI) = \log(m) + \rho \times \log(S_{LC}) \quad (3)$$

Figure 6 (top panel) shows the CTI calculated from Eq.(3) for each amplifier as function of signal level S_{LC} (in e^-), where different symbols show the CTI measurements for all four amplifiers - the asterisk symbols are for amplifier A , diamonds for amplifier B , triangles and squares are for amplifiers C & D respectively. The red symbols are the averaged CTI of the four amplifiers and the solid red line is the best linear fit of Eq.(3).

The middle panel of Figure 6 shows that the parameter ρ (the slope of the \log - \log CTI) *vs.* the time of observations is relatively constant over time for WFC3, at the level of ~ -0.68 . The value of ρ has been time-independent in other HST CCDs as well, implying that this parameter may be a measure of detector characteristic(s) intrinsic to the device, i.e., established during the manufacturing process. For comparison, the value of ρ was measured at -0.61 and -0.85 for ACS/WFC and HRC, respectively (Mutchler & Sirianni, 2005) and -0.82 for STIS (Goudfrooij *et al.*, 2006). There is no value ρ for WFPC2 as those chips were not able to take images in EPER-format.

The bottom panel of Figure 6 shows the m parameter (intercept of the \log - \log CTI) *vs.* time. The over-plotted best linear fit (black solid line) shows that CTI is increasing over time as the CTE decreases. However, the EPER observations taken right after the SMOV (July and August 2009, $MJD \lesssim 55.2$), seen in the middle panel and bottom panel of Figure 6, show large scatter in comparison with EPER measurements with the observations after that (the year of 2010, $55.2 \lesssim MJD \lesssim 55.4$). The cause of the higher scatter in early observations are due to the electronic noise with largest amplitudes. These low-level periodic noise component is still under investigation.

The over-plotted best linear fits show that $\log(m)$ is increasing over time as the CTE decreasing. However, the EPER measurements in 2011 indicate a slower decline in CTE than early EPER measurements from 2009 to the end of 2010 ($55.2 \lesssim MJD \lesssim 55.4$). The slower decline of CTE degradation may be due to changes in solar activity which affect the SAA (South Atlantic Anomaly), where most traps are thought to form. During periods of solar minimum e.g. 2009-2010, the SAA is stronger and more extended than during more active solar time periods, resulting in more traps and a faster CTE decline (Baggett *et al.*, 2011). Similar results have been found in the external CTE calibrations using the observations of globular cluster *47 Tuc* (K. Noeske *et al.* 2011).

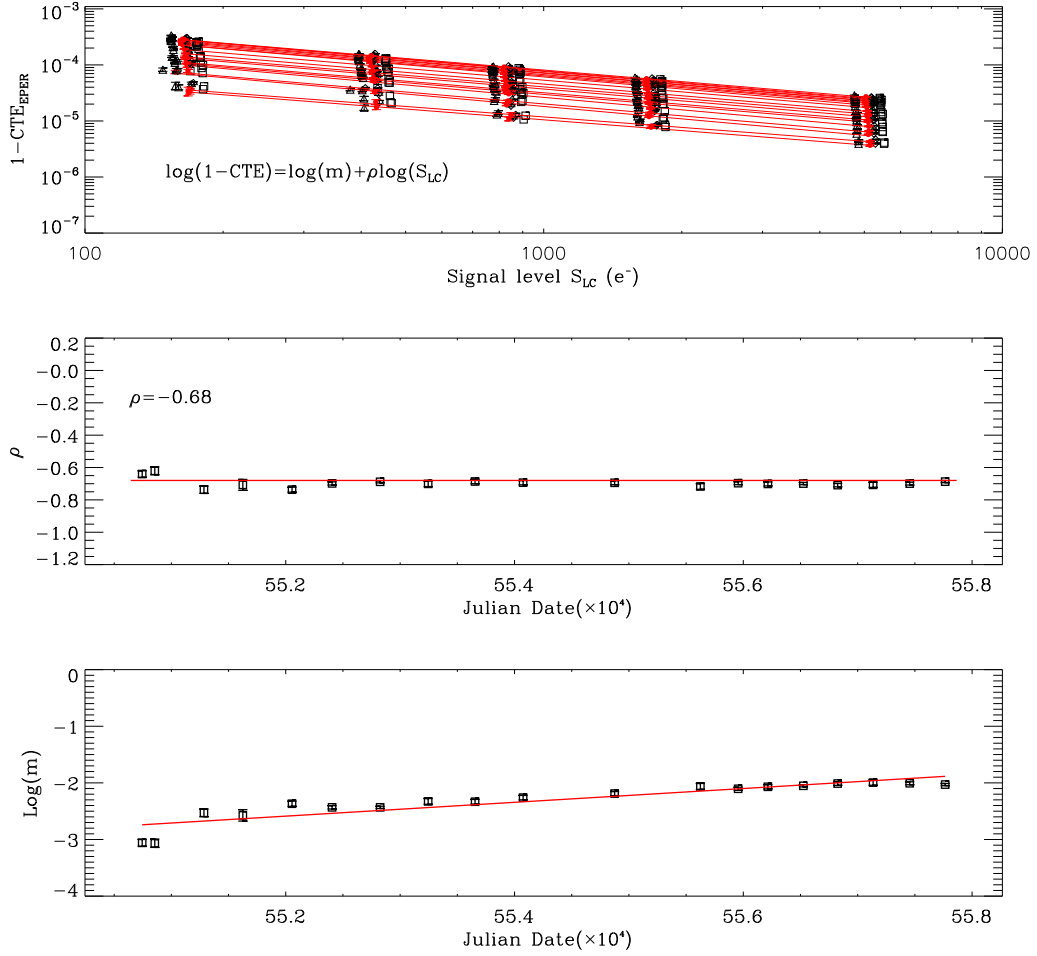


Fig. 6.— The top panel shows the *log-log* plot of CTI *vs.* signal level S_{LC} ; the solid red lines are the best linear fit. The middle panel shows ρ parameter *vs.* time (Modified Julian Date MJD); the over-plotted red line is the best linear fit. The bottom panel shows m as function of MJD with over-plotted red line as the best linear fit for all observations over 2 years.

Furthermore, the the WFC3/UVIS CTE measurements can be presented for each signal level as function of time. Figure 7 shows the WFC3 UVIS EPER CTE measurements at several signal levels over time and leads to the following conclusions:

- CTE declines linearly with time for all signal levels;
- lower signal levels have large measurement uncertainties compared with higher signal levels;
- lower signal levels suffer more CTE loss than higher signal levels.

For example, the measured UVIS CTE in August 2011 (MJD ~ 55.8) is 0.9997 for signal level of $\sim 160e^-$ and 0.99997 for signal level of $\sim 50000e^-$. A similar correlation of CTE loss as function of signal level was seen in ACS/WFC (see Figure 7 in Mutchler & Siriani, 2005).

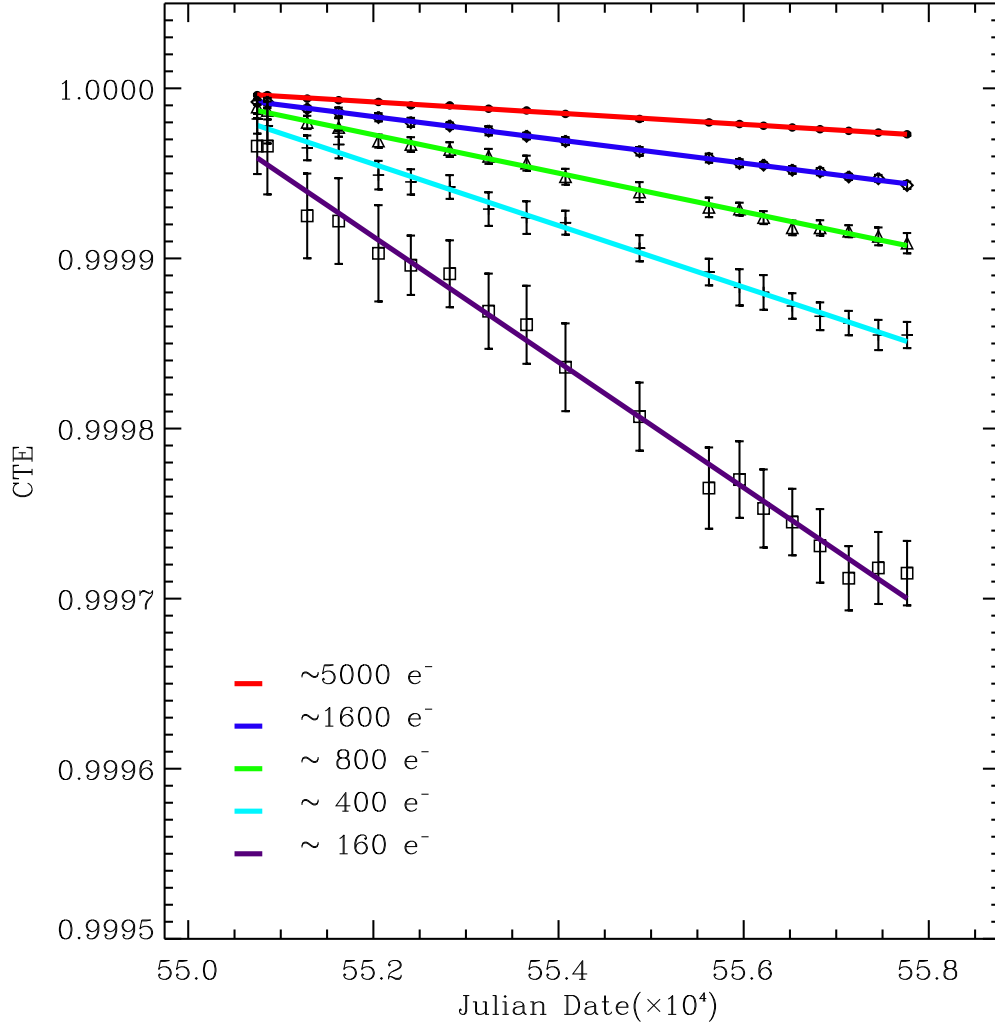


Fig. 7.— WFC3 UVIS parallel EPER measurements at selected signal levels *vs.* time (MJD). The best linear fit for different signal levels is over-plotted by different color lines.

4. Conclusion

The EPER method, which assesses the CTE level utilizing the trailing overscan in EPER-format images, measures CCD CTE losses *via* internal exposures. The advantage of this method is that it does not require the use of valuable external observing time and thus it is an effective, low-impact way to monitor the CTE over time. The internal calibration of CTE however, does not lead directly to corrections for stellar photometry due to CTI induced flux losses or corrections in stellar astrometry due to CTI induced centroid shift. Development of such a correction requires external observations of stellar cluster, for example. The EPER results are useful, however, for a relative measure of the CTE performance within a given instrument, in this case, WFC3. The WFC3/UVIS CTE degradation will continue to be monitored with both internal and external observations.

One way to mitigate CTI can be achieved by invoking the WFC3 charge injection capability. Analogous to the ACS/WFC pre-flash mode, the charge is injected before the science observation, albeit electronically rather than optically, in order to temporarily fill the traps causing the CTI. There will be a noise penalty although it is significantly lower than photon shot noise ($15e^-$ for 10,000 e^- injection; Giavalisco 2003). The charge injection capability is available as an observing option in Cycle 19. Further discussion of WFC3/UVIS CTE, CTI mitigation options, and results from external observations, can be found in the WhitePaper (Baggett, *et.al*, 2011) and in http://www.stsci.edu/hst/wfc3/ins_performance/CTE/.

WFC3/UVIS EPER measurements spanning almost 2 years have been presented here. These results have shown that the CTE behavior at low and high signal levels are similar to the corresponding ACS/WFC EPER measurements during its first year of its operation.

Acknowledgments

We are grateful to Howard Bushouse for a prompt and comprehensive review of this ISR. His helpful comments and suggestions have significantly improved the ISR.

References

- Anderson, J., Beddin, L., 2010, PASP, 122, pp.1035-1064
- Baggett, S., Bushouse, H., Gilliland, R., Kozhurina-Platais, V., Noeske, K., Petro, L., 2011, 2011, in “http://www.stsci.edu/hst/wfc3/ins_performance/CTE/CTE.pdf”
- Dressel, L., et al. 2010, ”Wide Field Camera 3 Instrument Handbook for Cycle 19, Version 3.0” (Baltimore: STScI)

- Chiaberge, M., Lim, P.M., Kozhurina-Platais, V., Sirianni, M., Mack, J., 2009, ACS Science Instrument Report 2009-01, (Baltimore: STScI)
- Dolphin, A. E., 2000, PASP, 112, 1397
- Gilliland, R., Goudfrooij, P., Kimble, R., 1999, PASP, 111, 1009
- Goudfrooij, P., & Kimble, R. A., 2003, in “2002 HST Calibration Workshop”, eds. A. Arribas, A. Koekemoer, & B. C. Whitmore (Baltimore: STScI), p.105
- Goudfrooij, P., Bohlin, R. C., & Maíz Apellániz, J., 2006, PASP, 118, 1455
- Janesick, J.R., 2001, “Scientific Charge-Coupled Devices”, SPIE Press, Bellingham VA
- Kozhurina-Platais, V., Goudfroij P., Puzia, T., 2007, ACS Science Instrument Report 2007-04, (Baltimore: STScI)
- Kozhurina-Platais, V., Sirianni, M., Chiaberge, M., 2008, in “Proceedings of IAU Symposium”, Vol. 248, p.272-273
- Kozhurina-Platais, V., Hilbert, B., Martel, A., McCullough, P., 2009, WFC3 Instrument Report 2009-11, (Baltimore: STScI)
- Kozhurina-Platais, V., Gilliland, R., Baggett, S., 2011, WFC3 Instrument Report 2011-06, (Baltimore: STScI)
- Markwardt, G. B., in “<http://cow.physics.wisc.edu/craigm/idl/idl.html>”
- Mutchler, M., & Sirianni, M., 2005, , ACS Science Instrument Report 2005-17 (Baltimore: STScI)
- Noeske, K., *et al*, 2011, in “<http://www.stsci.edu/hst/wfc3/insperformance/CTE/>”
- Riess, A., 2003, ACS Science Instrument Report 2003-09 (Baltimore: STScI)
- Riess, A., & Mack, J., 2004, ACS Science Instrument Report 2004-06 (Baltimore: STScI)
- Robberto, M., 2007, WFC3 Science Instrument Report 2007-13,(Baltimore: STScI)
- Whitmore, B. C., Heyer, I., & Casertano, S., 1999, PASP, 111, 1539